J Geophys (1984) 55:13–22

Journal of Geophysics

The crustal structure of the southern Rhinegraben from re-interpretation of seismic refraction data[1]

J.J. Zucca*

Geophysical Institute, University Karlsruhe, Hertzstraße 16, D-7500 Karlsruhe 21, Federal Republic of Germany

Abstract. The Rhinegraben is one of the best studied rift structures in the world. In the past 20 years, it has been the site of many seismic refraction studies. However, most of the profiles have only been interpreted using 1-D methods. In this paper a combined 2-D and 1-D analysis of the only reversed profile within the graben proper is presented. The new interpretation has resulted in changes in the *P*-wave velocity model of the Rhinegraben.

In the new model, the upper crust of the graben, representing the sedimentary graben-fill, is found to be 6–7 km thick with V_p less than 6.0 km/s. The mid-crust, which is probably of granitic/gneissic composition, shows a practically constant velocity of 6.25 km/s. This observation is supported by seismic reflection data. At the base of the crust is a velocity discontinuity followed by a 1.5 km thick transition zone into the upper mantle. From north to south along the graben, the crust thins by 3 km and the upper mantle velocity changes from about 8.4 km/s to 7.9 km/s.

In comparison with the old 1-D model, the new model shows a simplification of the structure of the lower crust and a thinning of the crust/mantle transition zone from 5 km to 1.5 km. Furthermore, in the old model, the upper mantle velocity underneath the graben was found to be constant at 8.1 km/s, which is in contrast to the changing upper mantle velocity found in the new model.

Key words: Rhinegraben – Crustal structure – Refraction seismology – Crust-mantle transition

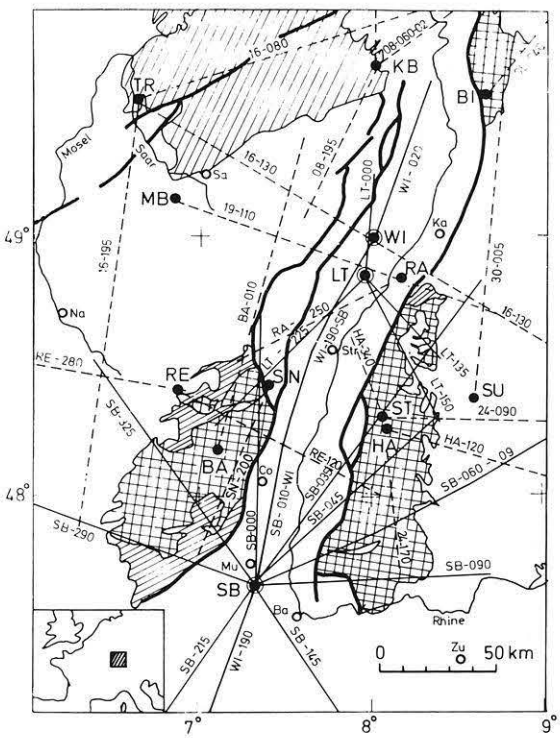

Fig. 1. Location map of seismic refraction profiles in the central and southern Rhinegraben (from Edel et al., 1975). *Closed dots:* shot points. *Open dots:* cities (Ka = Karlsruhe, Ba = Basel, Str = Strasbourg, Zu = Zürich, Mu = Mulhouse, Co = Colmar, Na = Nancy, Sa = Saarbrücken). *Thick lines:* boundary faults of the Rhinegraben. *Thin solid and dashed lines:* seismic refraction profiles. *Cross hatching:* crystalline rocks of the Rhenish Massif (north of the Rhinegraben), Vosges Forest (west of the Rhinegraben), and Black Forest (east of the Rhinegraben). The profile considered in this paper runs between shot points WI and SB (labelled: SB-010-WI and WI-190-SB)

Introduction

The Rhinegraben of central Europe (Fig. 1) is one of the best studied continental rifts in the world. Seismic refraction investigations, in particular, have a long history in the graben. Individual works can be found in the volumes: *The Rhinegraben Progress Report* (Rothe and Sauer, 1967), *Graben Problems* (Illies and Mueller, 1970) and *Approaches to Taphrogenesis* (Illies and Fuchs, 1974). A history of the seismic refraction work done in the Rhinegraben up to 1976 is given by Prodehl et al. (1976).

This paper deals with the re-interpretation of the only reversed, crustal, seismic refraction profile in the southern Rhinegraben (R.G.), namely, the profile from Wissembourg (WI) in the north to Steinbrunn (SB) in the south (Fig. 1). The Rhinegraben Research Group for Explosion Seismology (1974) was first to publish an interpretation of the WI-SB profile. Edel et al. (1975) was the next group to interpret these data. They presented an interpretation of the profile within the framework of all the other profiles shown in Fig. 1.

In this paper, a new development is added to the history

1 Contribution no. 276(56/SFB 108), Geophysical Institute, University of Karlsruhe

* *Present address:* Lawrence Livermore National Laboratory, Box 808, L-202, Livermore, CA 94550, USA

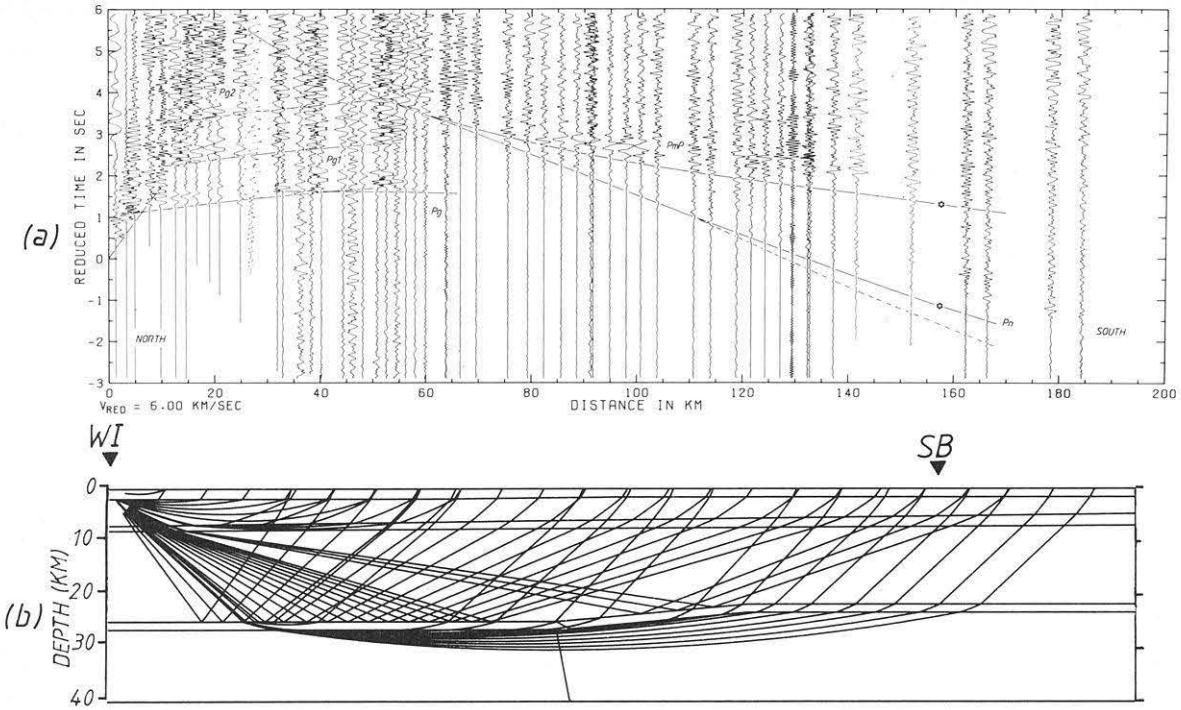

Fig. 2a and b. The data from shot point WI. **a** Trace-normalized record section. The *solid lines* (broken at the seismograms) represent the calculated travel times for the model shown in Fig. 6. The *dotted lines* are the calculated travel times for the model published by Edel et al. (1975). The *dotted/dashed lines* are a special case of the model in Fig. 6. The stars indicate reciprocal times. **b** Ray diagram. The model is the same as in Fig. 6 except no vertical exaggeration. Note: The model is only well controlled in areas penetrated by rays

of these data. Since the last interpretation of the profile, new techniques have become available which allow more detailed analysis of refraction data. In particular, I have done a 2-D analysis of the travel times. This is a marked improvement over the previous study, since the data from WI and SB were considered separately as two unreversed profiles. Ray theoretical amplitude data were also calculated, but because of a limitation inherent in ray theory, the results near the critical point are significantly in error. However, as discussed below, this problem can be sidestepped by using the ray theoretical amplitudes to make a comparison of the complete 2-D model with 1-D approximations. In the case of the Rhinegraben, the amplitudes may be interpreted with the more accurate reflectivity method.

I restrict my attention here to the WI-SB profile. It is also important to consider the other profiles in the area. However, they are unreversed and the application of 2-D methods will not significantly improve their interpretation.

Data

The data used in this interpretation are shown in Figs. 2a and 3a. These are normalized record sections. This means that the amplitude of each seismogram is individually scaled to a maximum width (amplitude) and that the same maximum width is used for every trace.

The way in which the interpreter correlates the seismic phases determines, to a large extent, how his final model will look. Different interpreters will sometimes interpret the same phase slightly differently. Therefore, in order to make clear the differences between the present model and that of Edel et al. (1975)[1], the travel times computed from Edel's published velocity-depth curves are included with the computed travel times from this study, which are all drawn together on top of the observed data in Figs. 2a and 3a.

Three main phases are observed on the record sections. These are marked by a solid line that is broken at the seismograms in Figs. 2a and 3a. The correlation used by Edel et al. (1975) is shown by dotted lines. The phases have been identified as *Pg, Pn,* and *PmP*. A description of each phase follows.

Pg

The apparent velocity of this phase starts low, about 3.2 km/s at WI and about 4.2 km/s at SB. The apparent velocity increases with increasing distance in a series of three steps until a maximum velocity of about 6.2 km/s is reached at an epicentral distance of about 60 km for both profiles. At this point the amplitude of *Pg* on both profiles drops sharply. It is difficult to trace *Pg* much beyond 65 km.

On the WI profile (Fig. 2a), at least two other phases can be seen which follow the *Pg* phase. They are labelled *Pg1* and *Pg2*. They have the same apparent velocity as the second segment of the *Pg* phase, follow at about 1.0 s and 2.0 s, respectively, behind the *Pg* phase, and are displaced slightly to larger distances.

PmP

This phase is recorded quite clearly on both record sections, although its precise correlation is difficult. Tracing the

1 Because of this comparison, it is necessary to refer to the work of Edel et al. (1975) rather frequently. In the rest of the paper I simply refer to "Edel" or "the old interpretation"

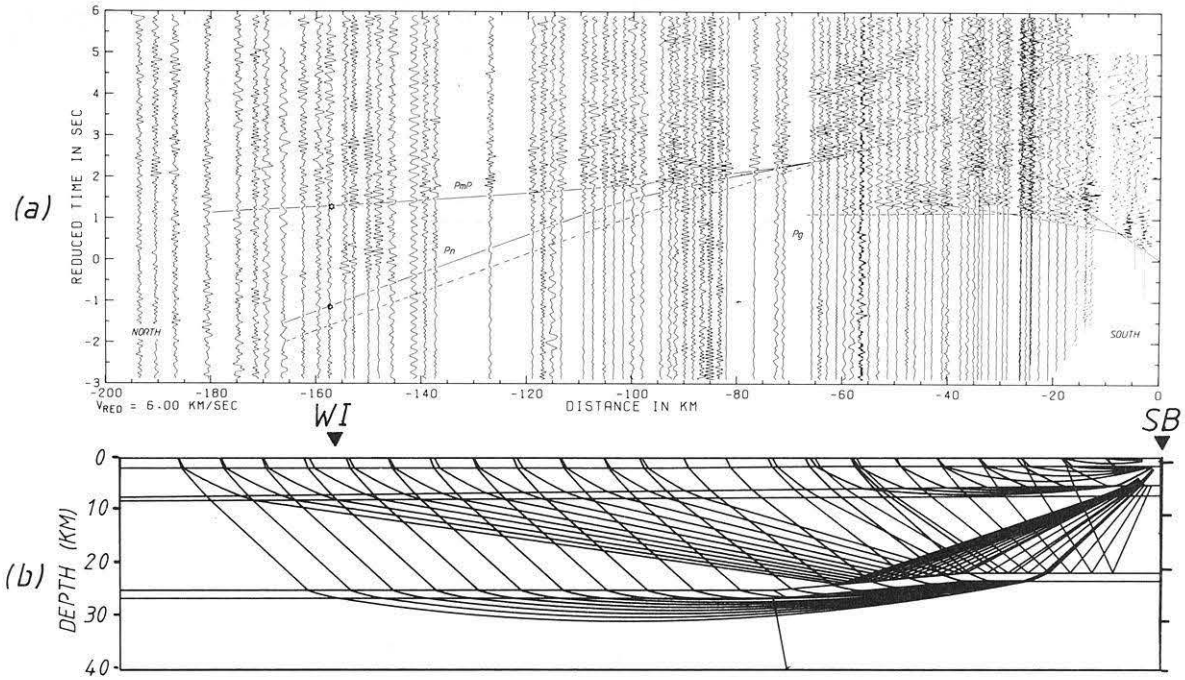

Fig. 3a and b. The data from shot point SB. **a** Trace-normalized record section. Same explanation as for Fig. 2. **b** Ray diagram. Same explanation as for Fig. 2

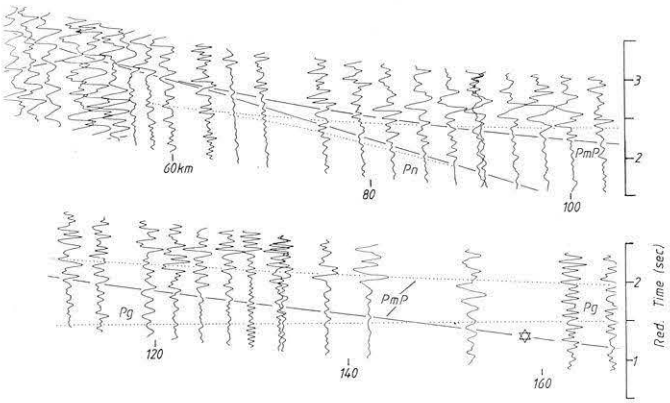

Fig. 4. Enlargement of the *PmP* correlation from shot point WI. *Solid lines:* the present correlation. *Dotted lines:* the previous correlation. The travel time branches that are not *PmP* are marked. The *star* indicates the *PmP* reciprocal time measured from the data from shot point SB

phase towards decreasing epicentral distances in the WI profile (Fig. 2a), *PmP* is at first clearly observed at an epicentral distance of 140 km and can be traced backwards to epicentral distances of less than 60 km. Figure 4 shows the correlation of the *PmP* phase between 60 and 140 km epicentral distance, on a greater scale. At 85 km, the present and previous correlations agree. At increasing epicentral distances the present correlation is earlier than the previous one. Without other information, it is difficult in Fig. 4 to decide which correlation fits the data better. In the distance range 100–130 km, the present correlation clearly fits the onset of the wavelet better than the previous correlation. However, in the distance range 130–150 km, the previous correlation provides the better fit. The *PmP* wavelet is very complicated across the length of Fig. 4 and it is difficult to determine if the old and new correlations represent different phases or only different ways to correlate the same phase. The previous correlation tends to follow the amplitude maximum of the wavelet while the present one tends to follow more the onset of the wavelet.

The apparent ambiguity can be resolved by consideration of the *PmP* reciprocal point. In Fig. 3a, the *PmP* reciprocal time is denoted by a star located over the position of the WI shot point. The nearest clear *PmP* arrivals are about 5 km away, at approximately 153 and 154 km epicentral distance. These arrivals constrain the *PmP* reciprocal time to 1.25 ± 0.15 s reduced time. The reciprocal time is plotted in Fig. 4 (and Fig. 2a) also as a star. It is clear that the reciprocal time supports the present correlation.

At epicentral distances less than 85 km in Fig. 4, the present correlation is later than the previous one. The later arrivals are approximately twice as large as the earlier ones. This is in the region of the critical point for this branch, where *PmP* should be its most impulsive. Therefore, the later, stronger arrivals are the best choice for the location of the *PmP* branch in this region.

In the SB record section (Fig. 3), the *PmP* phase is first clearly observed at an epicentral distance of about 160 km. It can then be traced back very clearly to about 60 km, where, with some imagination, it can be traced back even further to an epicentral distance of about 40 km. Note that the old and the new correlations are essentially the same.

Pn

From WI (Fig. 2a) this phase can be clearly observed as separate from the *PmP* phase at about 75 km epicentral distance. With increasing distance, *Pn* is clearly recorded out to about 135 km. Beyond 135 km epicentral distance, *Pn* becomes very difficult to correlate clearly. An important observation is that the *Pn* phase starts out at a high apparent velocity (8.5 km/s) where it separates from the *PmP* phase. It then slows down to a lower apparent velocity

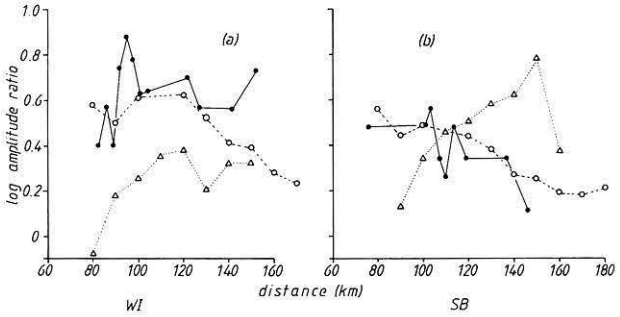

Fig. 5a and b. Log (base 10) *PmP/Pn* amplitude ratios. *Closed circles with solid lines:* observed data. *Open circles with dashed lines:* computed data using the reflectivity method on the 1-D velocity-depth functions shown in Fig. 5. *Open triangles with dotted lines:* computed data from Edel's models shown in Fig. 5. **a** Data for shot point WI. **b** Data for shot point SB

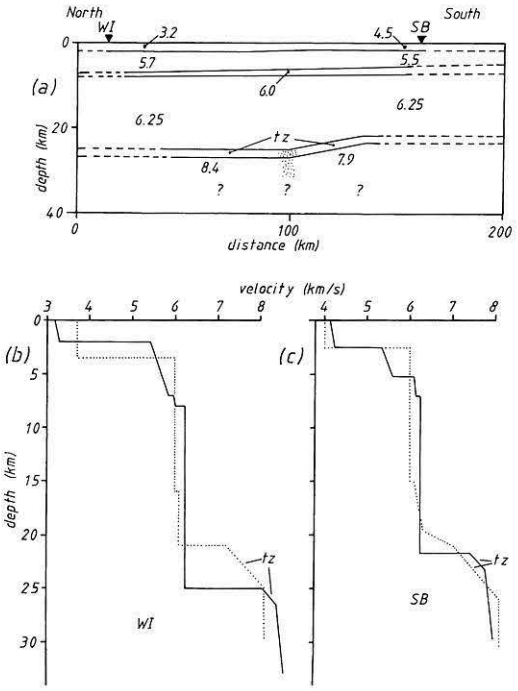

Fig. 6a, b and c. Velocity model for the WI-SB profile. **a** Two-dimensional model. The numbers displayed are *P*-wave velocities in km/s. The *stippled pattern* denotes a strong lateral change in velocity. The *dashed lines* indicate areas outside the control of the seismic data. 2:1 vertical exaggeration. **b** *Solid line:* velocity-depth function directly under shot point WI. *Dotted line:* velocity-depth function computed by Edel for shot point WI. "*tz*" denotes the transition zone beneath the base of the crust and upper mantle. **c** *Solid line:* velocity-depth function directly under shot point SB. *Dotted line:* velocity-depth function computed by Edel for the shot point SB. "*tz*" denotes the transition zone beneath the base of the crust and upper mantle

(8.15 km/s) beyond about 110 km. The old and the new correlations agree near where *Pn* and *PmP* separate, but the old correlation is about 0.2 s behind the new correlation between 120 and 130 km epicentral distance.

From SB (Fig. 3a), a similar pattern is also observed. The *Pn* phase is first clearly observed as separate from the *PmP* at about 95 km. Between this range and where it merges with *PmP*, *Pn* has an apparent velocity of 7.3 km/s. The *Pn* phase is most clearly observed between 95 and 120 km epicentral distance, where the phase changes to a higher apparent velocity of 8.5 km/s. The old correlation runs earlier than the new by about 0.3 s in this region. Note that this low apparent velocity to high apparent velocity change along the *Pn* branch is the opposite to that observed along the *Pn* branch from WI.

At the larger epicentral distances, the *Pn* branch is further constrained by the reciprocal times which are indicated by stars in Figs. 2a and 3a. The reciprocal time from shot point WI is reasonably well constrained by the good *Pn* arrival on the seismogram located at 152 km epicentral distance in Fig. 2a. In the data from shot point SB the reciprocal time provides the required control on the *Pn* branch at epicentral distances greater than 150 km.

Amplitudes

In this study, only the amplitude ratio of the *PmP* to *Pn* phase (Fig. 5) is considered in detail. The use of amplitude ratios is, in many respects, preferable to the use of true amplitudes. With amplitude ratios, the near-receiver effects are cancelled out and instrument/shot corrections do not need to be applied. However, since the ratio is a comparison, information is lost concerning the exact value of velocity gradients and steps. For example, in modelling a *PmP/Pn* ratio it is always possible to trade off the velocity difference at the Moho against the gradient of the underlying upper mantle. The WI-SB profile is made up of several shots which means that the amplitude of a phase cannot be carried across a series of stations into the next series of stations. Therefore, the true amplitude information is lost.

The amplitude ratios from WI (Fig. 5a) begin at 80 km epicentral distance with a log value of 0.4. At greater distances the curve jumps to higher values. The average value is about 0.6. The SB amplitude ratios (Fig. 5b) begin at a log value of 0.5 and then drop, with larger epicentral distances, to a final log value of about 0.15. An important thing to notice, concerning these data, is that the average amplitude ratio at WI (~0.6) is significantly greater than the average amplitude ratio at SB (~0.35).

Interpretation

The data have been interpreted with trial-and-error forward modelling. The computer programs used were SEIS81 (Červený and Pšenčík, 1981) for travel times and amplitudes in laterally varying media, and the reflectivity program (Fuchs and Müller, 1971) for amplitudes in one-dimensional media. Figure 6 shows the model that was calculated from the WI-SB profile. Figures 2b and 3b show the ray-paths through the models that were used to calculate the travel times and amplitudes. The correlations shown in Figs. 2a and 3a are the actual computed travel times from the model shown in Fig. 6 and from Edel's published results.

Pg

The *Pg* phase is the wave that travels through the upper part of the crust. In the Rhinegraben this means through the graben sediments and the upper part of the crystalline basement. The *Pg* phase has been modelled, from both WI and SB, by a stack of three layers that have constant velocity gradients. The disappearance of the *Pg* phase at epicen-

tral distances greater than 65 km is accomplished by the 6.25 km/s constant velocity layer and, because the record sections are normalized, the appearance of the *Pn*/*PmP* critical point, which is discussed in greater detail below.

At shotpoint WI, a *Pg1* and *Pg2* phase (Fig. 2a) is also observed in addition to the normal *Pg*. The travel times of the *Pg1* phase are well modelled by a free-surface reflection in the first layer followed by a refraction through the second layer. The travel times of the *Pg2* phase are well modelled by two free-surface reflections in layer one and then a refraction through the second layer. What is not well satisfied by this model are the amplitude ratios *Pg*/*Pg1* and *Pg*/*Pg2*. It is clear in Fig. 2a that *Pg1* has at least the same amplitude as *Pg*, if not greater. Amplitude modelling of the *Pg*/*Pg1* ratio produced a value of about 1.8. The observed value of *Pg*/*Pg1* is about 0.6 which is not in good agreement. Perhaps converted phases are somehow contributing to the amplitude, or there is some 3-D effect that cannot be taken into account. This aspect of the interpretation remains poorly resolved, but is not critical to the interpretation of the lower crustal structure.

The mid-crustal layer has been modelled with a 6.25 km/s velocity, which is somewhat higher than the 6.0 km/s velocity that was used in the old interpretation (Fig. 6a and b). This result comes from picking slightly faster arrivals than in the old interpretation. Edel points out that the *Pg* velocity used in the old study was meant to be an average for the whole R.G. area and as such would not be exact in specific instances.

PmP, Pn

The *PmP* phase is the wave that reflects from the crust/mantle interface. The *Pn* phase is the corresponding refraction through the underlying mantle. In general, I have correlated the same phases as Edel but in detail there are differences that lead to changes in the model. I have also changed the name of the reflected phase from a mid-crustal reflection to *PmP*. This is mostly a matter of semantics, but it alters the way one thinks about the structure.

As was mentioned above, the *Pn*/*PmP* critical point contributes to the abrupt disappearance of *Pg*. This is the case because the record sections are normalized. This means that the sudden appearance of a large amplitude phase would tend to reduce the amplitudes of the other arrivals on the trace. The modelled critical point is at 52 km epicentral distance for WI and 58 km epicentral distance for SB. The amplitude maximum for a *PmP* phase at about 7 Hz – the average frequency in both record sections – is shifted about 15 km away from the critical point towards increasing epicentral distances (Červený et al., 1977, p. 192). This places the amplitude maximum of *PmP* at around 70 km which is where the disappearance of the *Pg* phase should occur. This agrees well with what is observed in Figs. 2a and 3a.

In the WI profile, near the critical point, I correlate *PmP* 0.3 s later than Edel and also follow the phase back to epicentral distances less than the critical point, however, not with as much certainty. This difference in correlation results in the velocity step being located 4 km deeper than Edel calculated (Fig. 6b). From shot point SB, my *PmP* phase is almost exactly the same as the old correlation except I have correlated the phase back towards the source, past the critical point, although again without the same amount of certainty. The pre-critical reflection gives rise

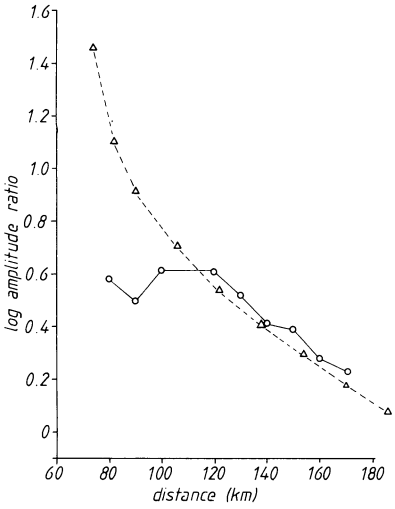

Fig. 7. Comparison of the *PmP*/*Pn* amplitude ratios using SEIS81 (*open triangles*) and the reflectivity method (*open circles*) on the velocity-depth function shown in Fig. 5b with the solid line. The frequency of the source wavelet is 5 Hz

to the velocity step in the present model, compared to the gradient zone in the old model (Fig. 6c). The modelling of the reflected phase controls the depth to the velocity step. Note that the step is located about 4 km deeper under WI than under SB.

An important feature of the new interpretation is the recognition that the *Pn* branch has two different phase velocities. This is partly a structural effect caused by the shallower Moho under shot point SB, but this alone is not enough to explain the data. To illustrate this point, the *Pn* branch is plotted in Figs. 2a and 3a as it would look if the upper mantle velocity under shot point WI were to extend to under shot point SB (dot-dashed lines). From shot point WI, the result is that the calculated *Pn* branch is about 0.3 s too early beyond 120 km epicentral distance. From shot point SB the result is that the computed *Pn* branch is about 0.3 s too early in the range 95–120 km epicentral distance, which is where the best arrival data are for the *Pn* branch from shot point SB. Therefore, to explain the data it is necessary to lower the velocity of the upper mantle beneath shot point SB. It is this aspect of the new interpretation that is 2-dimensional and cannot be modelled with 1-D methods. The lower velocity upper mantle under shot point SB results in a smaller velocity contrast across the Moho. As seen in the next section the smaller velocity contrast under shot point SB is also supported by the *PmP*/*Pn* amplitude ratio data.

Amplitude modelling of the PmP/Pn ratio

One problem in modelling these data is the shift of the maximum amplitude of the reflected phase away from the critical point. This effect is dependent on frequency and causes a discrepancy, near the critical point, between the ray method of synthetic seismogram calculation and more accurate methods such as reflectivity (Fuchs and Müller, 1971). Červený et al. (1977) and Červený (1979) discuss this problem in detail and propose corrections to the ray method for 1-D calculations. However, the correction has not been included in the two-dimensional amplitude calculations (SEIS81; Červený and Pšenčík, 1981).

An illustration of the discrepancy is shown in Fig. 7.

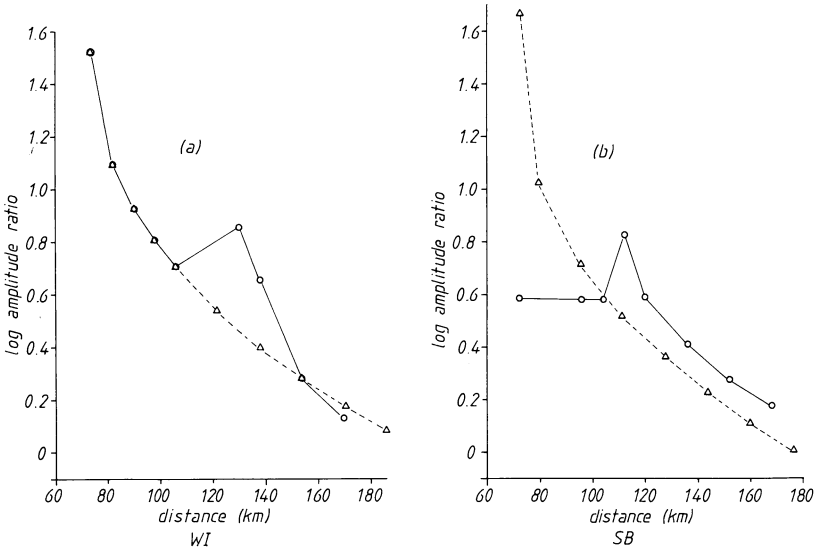

Fig. 8a and b. Comparison of the *PmP/Pn* amplitude ratios using SEIS81 in the 1-D and 2-D models. *Open triangles:* 1-D. *Open circles:* 2-D. **a** Ratios for WI. The 1-D model is shown by the solid line in Fig. 5. The 2-D model is shown in Figs. 6a and 2b. **b** Ratios for SB. The 1-D model is shown by the solid line in Fig. 5c. The 2-D model is shown in Figs. 6a and 3b

The *PmP/Pn* ratio is plotted for the 1-D structure under the WI shot point (Fig. 6b) using the reflectivity and ray methods. At distances greater than 120 km the two methods are in good agreement. At distances less than 120 km the two methods diverge sharply in their estimation of the *PmP/Pn* amplitude ratio. This presents a problem for the interpretation in this paper because the best amplitude data are located at distances less than 120 km.

The approach used to avoid this problem is to compare the 2-D synthetic seismograms with the 1-D synthetic seismograms to get a qualitative idea of how different the 1-D results are from the 2-D results. However, the final comparison of computed to observed amplitude data is done using the 1-D amplitude ratios calculated with the reflectivity method. Figures 6b and 6c are 1-D velocity-depth functions which show the velocity structure under shot points WI and SB respectively. Synthetic seismograms were calculated for the 1-D velocity-depth functions shown in Fig. 6b and c using SEIS81. The resulting *PmP/Pn* amplitude ratios are plotted in Fig. 8 with the triangles connected by dashed lines. Plotted in the same figure with open circles connected by solid lines are the *PmP/Pn* amplitude ratios calculated with SEIS81 for the shot points WI and SB in the 2-D velocity model in Fig. 6a. Qualitative comparison of the curves shown in Fig. 8 provides an estimation of how much the *PmP/Pn* amplitude ratio is affected by the 2-D structure.

At shot point WI (Fig. 6a) the structure is basically 1-D until the bend in the Moho is reached at about 100 km range. The 1-D amplitudes should be identical to the 2-D amplitudes up to the point where the rays start to pass through the bend in the Moho. Figure 8a shows this to be the case. (Note that 100 km range in Fig. 6a is 85 km epicentral distance in Fig. 8a.) The 1-D and 2-D amplitude ratios are identical up to about 105 km epicentral distance. At this point *PmP* rays in the 2-D model, which have been reflected off the up-turned part of the Moho, begin to arrive at the surface. This has the effect of focussing the *PmP* phase, which results in a higher *PmP/Pn* amplitude ratio. At the same time the *Pn* rays are travelling parallel to the up-turned part of the model which tends to scatter the *Pn* energy. Beyond the up-turned part of the Moho the *Pn* rays are re-focussed and the 2-D and 1-D *PmP/Pn* ratios are in rough agreement beyond 170 km epicentral distance in Fig. 8a.

At shot point SB (Fig. 6b) the rays are affected almost immediately by the bend in the Moho (Fig. 3b). The 1-D amplitudes should be different from the 2-D amplitudes over the whole range of observation. Figure 8b shows this result. At epicentral distances less than 105 km, the 1-D curve is greater than the 2-D curve. This is because the down-turn in the Moho in this range tends to scatter the *PmP* rays and focus the *Pn* rays (Fig. 3b). At epicentral distances greater than 105 km in Fig. 8b, the 2-D amplitude ratio becomes greater than the 1-D ratio. In this section the *Pn* rays are scattered by the flat Moho which allows the *PmP/Pn* amplitude ratio to rise again.

The main effect of the 2-D nature of the model is to flatten out the *PmP/Pn* amplitude ratio curves. What this means is that the tail of the curve is raised, or that the front is lowered, with respect to the average value of the amplitude ratio. However, this average value is not changed significantly and therefore, one may conclude that the *PmP/Pn* amplitude ratios are not changed significantly when the model is considered as two 1-D models as opposed to one 2-D model. This approach is *not* valid for the travel time analysis. In this case, the data could not have been accurately modelled had a 1-D travel time method been employed.

Figure 5 shows the observed amplitude ratios (closed circles) plotted with the calculated amplitude ratios (open circles) for shot points WI and SB. The agreement between the observed and computed data is quite reasonable given the scatter in the observed data. The *PmP/Pn* ratios computed from Edel's models (open triangles) are also added for comparison.

The difference in average value of the *PmP/Pn* ratio is caused by the difference in size of the velocity step under WI and SB. This provides additional evidence to support the interpretation that the mantle velocity is lower under the southern part of the R.G. Note that the amplitude ratios calculated from the old model do not successfully explain this feature of the data.

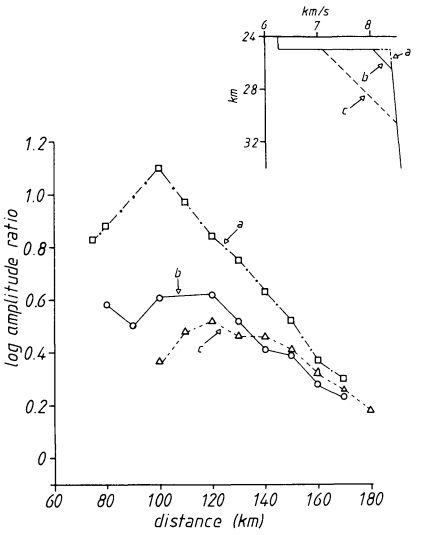

Fig. 9. Comparison of *PmP/Pn* amplitude ratios computed with the reflectivity method for varying thickness of the transition zone. The inset shows the velocity-depth structure of the various transition zones. "*a*": no transition zone. "*b*": 1.5 km thick transition zone (this curve is the part of the solid line velocity-depth function shown in Fig. 5b). "*c*": 5 km thick transition zone

Discussion

Transition zone

A major difference between the present model and Edel's model is in the structure of the lower crust and, in particular, the structure of the transition zone (labelled "*tz*" in Fig. 6b and c) between the upper mantle and lower crust. The same velocity gradient has been found as in the old study, but the thickness of this zone has now shrunk from about 5 km to 1.5 km.

Lower-crustal transition zones have been found in many of the world's rifts. Mooney et al. (1983) and Perathoner et al. (1981), besides interpreting new data, also present reviews of the crustal structure of various rift zones throughout the world. One feature that appears in all these studies is a layer at the base of the crust with a velocity of approximately 7.2 km/s that forms a transition between the crust and upper mantle. The transition zone is apparently confined to the rift zone proper. Because this feature is important to the tectonic understanding of rift zones, it is worthwhile to discuss the exact nature of the evidence for the existence of the transition zone in the Rhinegraben.

In the above mentioned studies, the transition zone manifests itself in a reflected or refracted phase that is observed on the record section. No such phase exists on the WI-SB profile in the Rhinegraben. The rays that travel through the transition zone in both the present model and Edel's model do not produce a separate phase. Instead, in both models, these rays arrive at the surface in a 5–10 km range and provide a smooth transition in the travel time curve between the critical point of the *PmP* reflection and the start of the *Pn* refraction. Given the distance spacing of 3–4 km between seismograms in the observed data, the presence and extent of the transition zone cannot be inferred from the travel time data. Amplitude data, instead, must be used to investigate the structure of the transition zone.

To test the effect of changing the thickness of the transition zone on the *PmP/Pn* amplitude ratio, a test was run. Figure 9 shows the results of this test. The bottom portion of the velocity-depth function below WI is shown in the inset as the solid line. The *PmP/Pn* ratio is plotted in the main part of the figure with the solid line. (This curve also appears in Fig. 5a.) Two other tests were made with variations of this strucutre: (1) no transition zone (labelled "*a*") and (2) 5 km transition zone (labelled "*c*"). The results show that in case "*a*" the amplitude ratio curve is quite peaked around 100 km. The 1.5 km transition zone (case "*b*") lowers this peak significantly. The 5 km transition (case "*c*") lowers the peak somewhat more. In terms of the observed data in Fig. 5, it is possible to distinguish between case "*a*" and "*b*" but there is no significant difference between "*b*" and "*c*". I conclude that the amplitude data require a transition zone that is at least 1.5 km thick. However, the thickness of the transition zone affects the travel time curves by moving the location of the critical point of the *PmP* reflection. It is important to fit the location of the critical point carefully because if improperly located, a poor fit to the corresponding refracted phase will result. In the present model, the best fit to the critical points and amplitude data is provided by the model with the 1.5 km thick transition zone.

Upper mantle velocity

Another major difference between the new model and Edel's is the change of upper mantle velocity along the profile. It is widely thought that the upward movement of mantle material and the subsequent heating of the crust and upper mantle is somehow related to graben formation (Fuchs, 1974; Mueller, 1978). There is no reason to expect that this heating takes place uniformly along the length of the graben. The evidence presented here for a smaller, upper mantle, *P*-wave velocity in the southern part of the Rhinegraben suggests that the heating process was most intense in the south. There are other geological and geophysical studies, which are discussed below, that support this interpretation.

The maximum uplift of the flanks of the graben occurred in the southern segment. This is clearly seen in Fig. 1. In the south, the flanks have been uplifted and eroded to expose the crystalline rocks of the Black and Vosges forests. The change from high to low velocity upper mantle occurs about 15 km south of Strasbourg. This roughly coincides with the northern border of the Vosges forest as shown in Fig. 1. In a review of Rhinegraben rifting, Illies (1978) proposed that a mantle diapir or plume ascended underneath the graben and that this plume came closest to the surface below the southern portion of the graben. The emplacement of the diapir at shallower depths beneath the southern part of the Rhinegraben could explain the enhanced shoulder uplift and lower velocity upper mantle in the south.

Werner and Kahle (1980) and Kahle and Werner (1980) used the hypothesis of rising mantle material to calculate the thermal regime under the R.G. They checked their results by computing the expected gravity field from the thermal effect and comparing it with the observed bouguer anomaly. Figure 8 of Kahle and Werner (1980, not reproduced here) summarizes their results. The figure shows two gravity profiles which lie across the graben. The first profile

is north of Strasbourg in the region of high upper mantle velocity and the second profile is south of Strasbourg in the region of low upper mantle velocity. They compare their computed gravity to the observed gravity and find a good fit, but in the north the computed gravity falls slightly below the observed (i.e., the thermal effect is overestimated) and in the south the computed gravity falls slightly above the observed (i.e. the thermal effect is underestimated). If Kahle and Werner had not used a uniform heating source under the graben, but a model where the heating was more intense in the south, the model would have predicted the data even more closely.

Panza et al. (1980) have calculated upper mantle and asthenosphere *S*-wave velocities in Europe by analysis of surface wave data. Their results provide only the gross features of the lithosphere/asthenosphere structure in Europe, but they suggest that there is a lowering of the *S*-wave velocity in the asthenosphere below the southern segment of the graben.

In the above discussion, the actual values of the upper mantle *P*-wave velocities have not been empasized. Instead, the independent evidence for changes in the nature of the upper mantle along the Rhinegraben have been discussed. The velocity change of 7.9–8.4 km/s is very large and in fact 8.4 km/s seems strangely high for an upper mantle *P*-wave velocity, although similar velocities have been recorded for the upper mantle from long-range profiles in southern Germany (Ansorge et al. 1979). In reality, the upper mantle velocity is poorly constrained because of the shallowing of the *M*-discontinuity from north to south. A shot point in the middle of the WI-SB profile is needed to provide true reversal of the upper mantle velocities calculated here. However, the data presented clearly suggest that the crustal structure of the southern Rhinegraben is different from the crustal structure in the north. One way to explain this difference in structure is to have more intense heating and mantle rise in the south compared to the north during the formation of the graben.

Geological interpretation

The results computed here can be combined with the results from other profiles in the southern Rhinegraben area to produce a cross-section of the crust across the graben. Figure 10 shows this result. The profile runs perpendicular to the graben axis approximately 40 km north of the SB shot point between the Vosges and Black forests. The precise location of the cross-section is not shown on Fig. 1 because the profile shown in Fig. 10 is only a schematic. The results from the profiles BA-010, SB-035, and SB-045 presented by Edel, which the author had a chance to check during the course of this work, are projected into the profile line. The same sort of schematic cross-section was used by Edel et al. (1975) to summarize their results.

On the flanks of the graben, gneisses and granites are exposed in the Black and Vosges forests (Walther and Zitzmann, 1981). These rocks have a much higher velocity than the graben-fill sediments. The boundary in the graben between the sediments and the crystalline basement is probably represented by the 5.4–6.0 km/s discontinuity shown in Fig. 10. The absence of structure in the mid-crust in the cross-section suggests that the same gneisses and granites that are exposed in the flanks of the graben probably exist underneath the graben as well. In fact these rocks probably

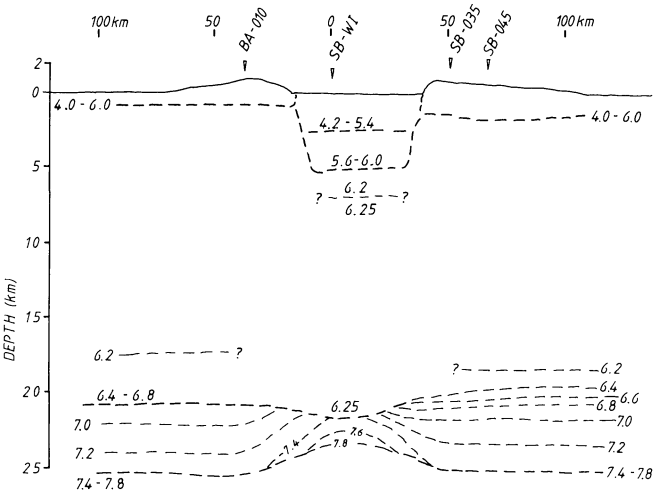

Fig. 10. Velocity-depth profile of the Rhinegraben drawn perpendicular to the axis of the graben approximately 40 km north of shot point SB. Contour interval: 0.2 km/s. Zero depth is unterstood to mean the floor of the graben

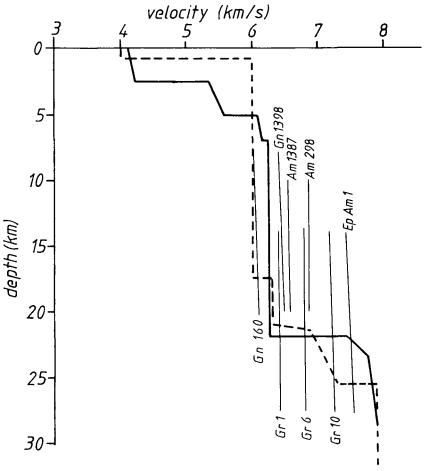

Fig. 11. Comparison of 1-d velocity-depth functions with laboratory measurements of crystalline rocks. For sample descriptions see Table 1. The samples published by Kern (1982) have been temperature-corrected using his published velocity/temperature derivatives. For the samples published by other authors, a V_p/T derivative of -2.50×10 E-4 km/s°C was used, which is approximately the average of all the V_p/T derivatives published by Kern (1982). Note: gn = gneiss; am = amphibolite. gr = granulite

extend to a depth of over 20 km in the crust, to the point where the velocity increases to 6.3 km/s.

Figure 11 supports this interpretation with laboratory measurements. In the figure, the velocity-depth functions from the profiles SB-WI and BA-010 (see Fig. 1 for profile location) have been plotted together with temperature-corrected velocity-depth curves of laboratory-measured rock samples. The purpose of this figure is to show a range of rock types that could produce a given velocity at a given depth in the R.G. Table 1 is a list of sources for the velocity, temperature and pressure data. The velocity-depth curves for the rock samples have been corrected for the 'warm' continental crustal geotherm of Theilen and Meissner (1979). The mid-crustal section of the velocity-depth curve for the WI-SB profile is bracketed by the Gn 160 and Gn 1398 curves. This suggests that gneiss is a plausible constitu-

Table 1. Composition and sources for experimental velocity-depth curves shown in Fig. 16

Gneiss 160:	47qu, 7plg, 28bi, 18ep (Kern, 1982)
Gneiss 1398:	33qu, 40plg, 3hbl, 16gar, 5px, 2or (Kern, 1982)
Amphibolite 1387:	43plg, 45hbl, 3mi, 3or, 5tit (Kern, 1982)
Amphibolite 298:	27qu, 18plg, 48hbl, 4eq, 2or, 1tit (Kern, 1982)
Amphibolite 1:	5qu, 11plg, 50hbl, 34ep (Christensen, 1965)
Granulite 1:	24qu, 67plg, 6px, 1mi (Christensen and Fountain, 1975)
Granulite 6:	2qu, 53plg, 22hbl, 18px, 3bi (Christensen and Fountain, 1975)
Granulite 10:	60pgl, 26px, Ogar (Christensen and Fountain, 1975)

Note: Modal analyses in percentages by volume: qu = quartz, plg = plagioclase, bi = biotite, hbl = hornblende, px = pyroxene, ep = epidote, gar = garnet, tit = titanite, mi = microcline, or = orthoclase

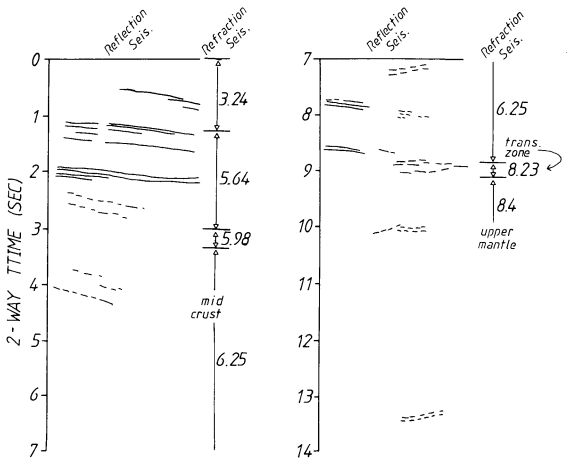

Fig. 12. Line drawing of the seismic reflection results from Dohr (1970) compared with the calculated seismic refraction results from this paper. The numbers written between the intervals in the refraction seismic part are the average velocity for that interval in km/s used to calculated the two-way travel time through the refraction model

ent of the crust of the R.G. This is a very reasonable interpretation in view of the gneisses that outcrop in the Vosges and Black forests on the graben's flanks. Note also that the laboratory-measured samples show very little change of velocity with depth. The velocity-depth curve of the mid-crust in the R.G. also has a very small gradient, which suggests that the gneisses that compose the crust of the R.G. have relatively constant composition with depth.

At depths greater than 22 km on the flanks of the graben the velocity increases, to an average of 7.1 km/s with a fairly high velocity gradient. For the change in velocity to represent only a phase change, the gneisses would have to transform, for example, into an iron-, magnesium-poor granulite (gr 1 in Fig. 11) or amphibolite (amp 1387 in Fig. 11). However, the laboratory velocities of these rocks are not high enough to compare well with the observed velocities. The transition to the lower crust on the flanks of the Rhinegraben probably represents a compositional change, i.e., increasing iron and magnesium and also increasing metamorphic grade. In fact, the strong gradient in the lower crust suggests a continuing increase with depth of mafic mineral content in the lower crust.

Underneath the graben, the lower crustal layer thins out and the upper mantle and mid-crust appear to bulge into the lower crust. In other words, it appears that the lower crust under the graben has been attenuated and replaced with higher velocity material, probably derived from the mantle.

One striking feature of the model is the complete lack of structure in the mid-crust. Some independent evidence supporting this observation comes from the reflection data collected by Dohr (1970) near the city of Rastatt (RA in Fig. 1). A line drawing of these data appear in Fig. 12. At the side is the velocity-depth function for shot point WI computed in this paper converted to a time-section by simply computing 2-way travel times through the model. The velocity written next to the model represents the average velocity used for each interval. In the first 2.5 s of the data there are many strong reflections that correlate with the 3.24 and 5.64 km/s layers or, in other words, the material above the 5.6–6.0 km/s velocity discontinuity shown in Fig. 10. The 5.98 km/s interval represents a small transition into the 6.25 km/s mid-crust. The mid-crust is free of strong reflectors for over 4 s until the strong reflector at 7.8 s is reached. Further down in the section a band of reflections is observed from 7.2–9.0 s. The transition zone in the refraction model (layer with average velocity 8.23 km/s) occurs at the bottom of this band of reflections. The lack of reflections over an interval of 4 s supports the featureless mid-crust found in the refraction model. The failure of the refraction model to perfectly predict the transition zone shown in the reflection model suggests that the transition could be locally thickened under Rastatt. Another possibility is that the lower crust is laminated, as discussed by Deichmann and Ansorge (1983), and this lamination has been attenuated by the rifting process on a regional scale, but is still intact locally.

Conclusions

This report presents a re-interpretation of selected seismic refraction data from the area around the southern Rhinegraben. Through the use of 2-D travel time and 1-D amplitude interpretation techniques, and a slightly different phase correlation, the *P*-wave velocity model along the axis of the Rhinegraben has changed significantly.

The upper crust of the southern Rhinegraben area is interpreted to be of granitic/gneissic composition. These rocks probably extend to a depth of 20 km in the crust. In the graben itself, these rocks are covered by 6–7 km of graben-fill sediments. Below approximately 20 km is the lower crustal layer which, under the flanks of the graben, has a higher mafic component than the granites and gneisses found in the Black and Vosges forests. Under the graben proper, the lower crustal layer appears to be attenuated and enriched by even more mafic material, which was probably derived from the mantle during the formation of the graben.

Along the axis of the Rhinegraben the upper mantle *P*-wave velocity changes from 8.4 km/s in the north to 7.9 km/s in the south. Although the actual velocity of the upper mantle is poorly constrained, the data clearly indicate a difference in the upper mantle *P*-wave velocity along the axis of the graben. One way to explain this observation is to have more heating in the southern portion of the graben during its formation.

Acknowledgments. This work was supported by a research grant from the Fritz Thyssen Stiftung. The model calculations were done in the Computer Centre of the University of Karlsruhe, FRG. The data were plotted and processed on the computer facilities of the Geophysical Institute of the University of Karlsruhe with the kind help of Mickey Kaminski. Dr. Claus Prodehl provided the Rhinegraben data for me to work with and made possible my stay in Karlsruhe. Professor Dr. Karl Fuchs critically reviewed the manuscript. Dr. Jim Mechie also critically reviewed the manuscript and provided the author with many helpful suggestions and discussions during the course of the research.

References

Ansorge J., Bonjer, K.-P., Emter, D.: Structure of the uppermost mantle from long-range seismic observations in southern Germany and the Rhinegraben area. Tectonophysics **56**, 31–48, 1979

Ansorge, J., Emter, D., Fuchs, K., Lauer, J.P., Mueller, St., Peterschmidt, E.: Structure of the crust and upper mantle in the rift system around the Rhinegraben. In: Graben Problems, J.H. Illies and St. Mueller, eds.: pp 190–197. International Upper Mantle Project Sci. Rep. No. 27, Schweizerbart, 1970

Červený, V.: Accuracy of ray theoretical seismograms. J. Geophys. **46**, 135–149, 1979.

Červený, V., Pšenčík, I.: SEIS81, a 2-D seismic ray package. Charles University, Prague, 1981

Červený, V., Molotkov, I.A., Pšenčík, I.: Ray method in seismology. Charles University, Prague, 1977

Christensen, N.I.: Compressional wave velocities in metamorphic rocks at pressures to 10 kilobars. J. Geophys. Res. **70**, 6147–6164, 1965

Christensen, N.I., Fountain, D.M.: Constitution of the lower continental crust based on experimental studies of seismic velocities in granulite. Geol. Soc. Amer. Bull. **86**, 227–236, 1975

Deichman, N., Ansorge, J.: Evidence for lamination in the lower continental crust beneath the Black forest (Southwestern Germany). J. Geophys. **52**, 109–118, 1983

Dohr, G.: Reflexionsseismische Messungen im Oberrheingraben mit digitaler Aufzeichnungstechnik und Beobachtungen. In: Graben Problems, J.H. Illies and St. Mueller, eds.: pp 207–218. Int. Upper Mantle Proj. Sci. Rep. No. 27, Schweizerbart, 1970

Edel, J.B., Fuchs, K., Gelbke, C., Prodehl, C.: Deep structure of the southern Rhinegraben area from seismic refraction investigations. J. Geophys. **41**, 333–356, 1975

Fuchs, K.: Geophysical contributions to Taphrogenesis. In: Approaches to Taphrogenesis, J.H. Illies and K. Fuchs, eds.: pp 420–432. Inter-Union Commission on Geodynamics 1974

Fuchs, K., Müller, G.: Computation of synthetic seismograms with the reflectivity method and comparison with observations. Geophys. J.R. Astron. Soc. **23**, 417–433, 1971

Illies, J.H.: Two stages of Rhinegraben rifting. In: Tectonics and Geophysics of Continental Rifts, I.B. Ramberg and E.R. Neumann, eds.: pp 63–71. D. Reidel, 1978

Illies, J.H., Fuchs, K. (eds.): Approaches to Taphrogenesis, Inter-Union Commission on Geodynamics Sci. Rep. No. 8, Schweizerbart, 1974

Illies, J.H., Mueller, St. (eds.): Graben Problems, International Upper Mantle Project Sci. Rep. No. 27, Schweizerbart, 1970

Kahle, H.G., Werner, D.: A geophysical study of the Rhinegraben – II. Gravity anomalies and geothermal implications. Geophys. J.R. Astron. Soc. **62**, 631–647, 1980

Kern, H.: P- and S-wave velocities in crustal and mantle rocks under the simultaneous action of high confining pressure and high temperature and the effect of the rock microstructure. In: High Pressure Research in Geoscience, W. Schreyer, ed.: pp 13–45. Schweizerbart, 1982

Meissner, R., Vetter, U.: The northern end of the Rhinegraben due to some geophysical measurements. In: Approaches to Taphrogenesis, J.H. Illies and K. Fuchs, eds., pp 236–243. Inter-Union Commission on Geodynamics Sci. Rep. No. 8, Schweizerbart, 1974

Mooney, W.D., Andrews, M.C., Peters, D., Hamilton, R.M.: Crustal structure of the northern Mississippi Embayment and a comparison with other continental rift zones. Tectonophysics **94**, 327–348, 1983

Mueller, St.: A new model of the continental crust. In: The Earth's Crust. Amer. Geophys. Un. Monograph **20**, 289–317, 1977

Mueller, St.: Evolution of the earth's crust. In: Tectonics and Geophysics of Continental Rifts, J.B. Ramberg and E.R. Neumann, eds.: pp 11–28. Reidel, 1978

Panza, G.F., Mueller, St., Calcagnile, G.: The gross features of the lithosphere-asthenosphere system in Europe from seismic surface waves and body waves. Pageoph. **118**, 1209–1213, 1980

Perathoner, B., Fuchs, K., Prodehl, C., Ginzburg, A.: Seismic investigation of crust-mantle transition in continental rift systems – Jordan-Dead Sea Rift and Rhinegraben. Tectonophysics **80**, 121–133, 1981

Prodehl, C., Ansorge, J., Edel, J.B., Emter, D., Fuchs, K., Mueller, St., Peterschmidt, E.: Explosion-seismology research in the central and southern Rhinegraben – A case history. In: Explosion seismology in central Europe – data and results, P. Giese, C. Prodehl, A. Stein, eds.: pp 313–328. Springer-Verlag, 1976

Rhinegraben Research Group for Explosion Seismology: The 1972 Seismic Refraction Experiment in the Rhinegraben – First Results. In: Approaches to Taphrogenesis, J.H. Illies and K. Fuchs, eds.: pp 122–137. Inter-Union Commission on Geodynamics Sci. Rep. No. 8. 1974

Rothe, J.P., Sauer, K. (eds.): The Rhinegraben progress report, International Upper Mantle Project Sci. Rep. No. 13, 1967

Theilen, Fr., Meissner, R.: A comparison of crustal and upper mantle features in Fennoscandia and the Rhenish Shield, two areas of recent uplift. Tectonophysics **61**, 227–242, 1979

Walther, H.W., Zitzmann, A.: Geologische Karte der Bundesrepublik Deutschland 1:100000. Bundesanstalt für Geowissenschaften und Rohstoffe, Hannover, W. Germany, 1973, third edition, 1981

Werner, D., Kahle, H.G.: A geophysical study of the Rhinegraben – I. Kinematics and geothermics. Geophys. J.R. Astron. Soc. **62**, 617–629, 1980

Received October 17, 1983; Revised version April 13, 1984
Accepted April 16, 1984